FRB 121102 Bursts Show Complex Time–Frequency Structure

J. W. T. Hessels[1,2] , L. G. Spitler[3] , A. D. Seymour[4], J. M. Cordes[5] , D. Michilli[1,2] , R. S. Lynch[4,6] , K. Gourdji[2],
A. M. Archibald[1,2] , C. G. Bassa[1], G. C. Bower[7] , S. Chatterjee[5], L. Connor[1,2] , F. Crawford[8] , J. S. Deneva[9] , V. Gajjar[10] ,
V. M. Kaspi[11] , A. Keimpema[12] , C. J. Law[13] , B. Marcote[12] , M. A. McLaughlin[6,14] , Z. Paragi[12] , E. Petroff[1,2] ,
S. M. Ransom[15] , P. Scholz[16], B. W. Stappers[17], and S. P. Tendulkar[11]

[1] ASTRON, Netherlands Institute for Radio Astronomy, Oude Hoogeveensedijk 4, 7991 PD Dwingeloo, The Netherlands; J.W.T.Hessels@uva.nl
[2] Anton Pannekoek Institute for Astronomy, University of Amsterdam, Science Park 904, 1098 XH Amsterdam, The Netherlands
[3] Max-Planck-Institut für Radioastronomie, Auf dem Hügel 69, D-53121 Bonn, Germany
[4] Green Bank Observatory, P.O. Box 2, Green Bank, WV 24944, USA
[5] Cornell Center for Astrophysics and Planetary Science and Department of Astronomy, Cornell University, Ithaca, NY 14853, USA
[6] Center for Gravitational Waves and Cosmology, West Virginia University, Morgantown, WV 26506, USA
[7] Academia Sinica Institute of Astronomy and Astrophysics, 645 N. A'ohoku Place, Hilo, HI 96720, USA
[8] Department of Physics and Astronomy, Franklin and Marshall College, Lancaster, PA 17604-3003, USA
[9] George Mason University, resident at the Naval Research Laboratory, Washington, DC 20375, USA
[10] Space Sciences Laboratory, 7 Gauss way, University of California, Berkeley, CA 94720, USA
[11] Department of Physics and McGill Space Institute, McGill University, Montreal, QC, H3A 2T8, Canada
[12] Joint Institute for VLBI ERIC, Oude Hoogeveensedijk 4, 7991 PD Dwingeloo, The Netherlands
[13] Department of Astronomy and Radio Astronomy Lab, University of California, Berkeley, CA 94720, USA
[14] Department of Physics and Astronomy, West Virginia University, Morgantown, WV 26501, USA
[15] National Radio Astronomy Observatory, Charlottesville, VA 22903, USA
[16] Dominion Radio Astrophysical Observatory, Herzberg Astronomy & Astrophysics Research Centre, National Research Council Canada, P.O. Box 248, Penticton, V2A 6J9, Canada
[17] Jodrell Bank Center for Astrophysics, School of Physics and Astronomy, University of Manchester, Oxford Road Manchester, UK

Abstract

FRB 121102 is the only known repeating fast radio burst source. Here we analyze a wide-frequency-range (1–8 GHz) sample of high signal-to-noise, coherently dedispersed bursts detected using the Arecibo and Green Bank telescopes. These bursts reveal complex time–frequency structures that include subbursts with finite bandwidths. The frequency-dependent burst structure complicates the determination of a dispersion measure (DM); we argue that it is appropriate to use a DM metric that maximizes frequency-averaged pulse structure, as opposed to peak signal-to-noise, and find DM = 560.57 ± 0.07 pc cm^{-3} at MJD 57,644. After correcting for dispersive delay, we find that the subbursts have characteristic frequencies that typically drift lower at later times in the total burst envelope. In the 1.1–1.7 GHz band, the $\sim$0.5–1 ms subbursts have typical bandwidths ranging from 100 to 400 MHz, and a characteristic drift rate of $\sim$200 MHz ms^{-1} toward lower frequencies. At higher radio frequencies, the subburst bandwidths and drift rate are larger, on average. While these features could be intrinsic to the burst emission mechanism, they could also be imparted by propagation effects in the medium local to the source. Comparison of the burst DMs with previous values in the literature suggests an increase of ΔDM $\sim$ 1–3 pc cm^{-3} in 4 yr; though, this could be a stochastic variation as opposed to a secular trend. This implies changes in the local medium or an additional source of frequency-dependent delay. Overall, the results are consistent with previously proposed scenarios in which FRB 121102 is embedded in a dense nebula.

Key words: galaxies: dwarf – radiation mechanisms: non-thermal – radio continuum: general

1. Introduction

Fast radio bursts (FRBs) are short-duration astronomical radio flashes of apparent extragalactic origin (Lorimer et al. 2007; Thornton et al. 2013; Petroff et al. 2016). FRB emission arrives later at lower radio frequencies, and this has been attributed to dispersive delay from intervening ionized material. This dispersive delay is quadratic with radio frequency ($\Delta t \propto \nu^{-2}$), and its magnitude is proportional to the dispersion measure (DM), which is the column density of free electrons between source and observer. The large DMs of FRBs are inconsistent with models of the Galactic free electron density distribution (Cordes & Lazio 2002; Yao et al. 2017). This suggests that FRBs originate at extragalactic distances, because their anomalously large DMs cannot be explained by an additional dispersive delay from material local to a source in the Milky Way but can be explained by material in a host

galaxy and the intergalactic medium (Lorimer et al. 2007; Thornton et al. 2013).

Discovered in the Arecibo PALFA pulsar survey (Cordes et al. 2006; Lazarus et al. 2015), FRB 121102 is a source of sporadically repeating FRBs (Spitler et al. 2014, 2016; Scholz et al. 2016). The direct and precise localization of these bursts has shown that FRB 121102 is hosted in the star-forming region of a dwarf galaxy at a luminosity distance of $\sim$1 Gpc ($z = 0.193$; Bassa et al. 2017; Chatterjee et al. 2017; Marcote et al. 2017; Tendulkar et al. 2017). This association thus confirms the extragalactic distance of FRB 121102, as was previously inferred from its DM (Spitler et al. 2014). FRB 121102 is also associated with a compact (diameter $<$0.7 pc), persistent radio source with isotropic luminosity $L_{\rm radio} \sim 10^{39}$ erg s^{-1} (Chatterjee et al. 2017; Marcote et al. 2017). Deep X-ray and γ-ray observations have found no persistent high-energy counterpart to FRB 121102 (Scholz et al. 2017). Many models for FRB 121102 have focused on

a young, energetic, and highly magnetized neutron star origin (e.g., Connor et al. 2016; Cordes & Wasserman 2016; Lyutikov et al. 2016). FRB 121102's host galaxy is of a type that is also known to host superluminous supernovae and long gamma-ray bursts; as such, it has been suggested that FRB 121102 originates from a millisecond magnetar formed in the last few decades (Marcote et al. 2017; Metzger et al. 2017; Tendulkar et al. 2017). This scenario can also naturally explain the colocation of FRB 121102 with a star-forming region, as well as its association with the persistent radio source, which would represent a pulsar or magnetar wind nebula (PWN or MWN) and/or a supernova remnant (SNR; Murase et al. 2016; Piro 2016; Kashiyama & Murase 2017; Margalit et al. 2018).

As yet, no other FRB source has been seen to repeat, despite dedicated searches for additional bursts (e.g., Petroff et al. 2015b; Ravi et al. 2015; Shannon et al. 2018), nor are there any other definitive host galaxy associations. While Keane et al. (2016) present a potential afterglow to FRB 150418, Williams & Berger (2016) argue that the putative counterpart is unassociated variability of an active galactic nucleus in the same field (see also the discussion in Bassa et al. 2016; Johnston et al. 2017). Thus, it remains unclear whether FRB 121102 has a similar physical origin to other known FRBs (e.g., Ravi 2019).

Optical, X-ray, and γ-ray observations that are simultaneous with detected FRB 121102 radio bursts have failed to identify any prompt high-energy counterpart to the radio bursts themselves (DeLaunay et al. 2016; Hardy et al. 2017; Scholz et al. 2017). Given the absence of multiwavelength counterparts, the properties of the radio bursts are thus critical for understanding the emission mechanism (Lyubarsky 2014; Beloborodov 2017; Lyutikov 2017; Waxman 2017) and the local environment of the source through imparted propagation effects (Cordes et al. 2017). The bursts have typical durations of milliseconds, but also show fine structure as narrow as $\sim 30\,\mu$s (Michilli et al. 2018). The spectrum varies between bursts, even those that are separated by minutes or less (e.g., Figure 3 of Gajjar et al. 2018). Simultaneous, multitelescope data show that some bursts are visible over a relatively broad range of frequencies (>1 GHz, see Law et al. 2017). However, wide-band observations also show that many of the bursts peak in brightness within the observing band and are not well modeled by a power law (Scholz et al. 2016; Spitler et al. 2016).

Recently, the detection of FRB 121102 bursts at relatively high radio frequencies of 4–8 GHz has revealed that the bursts are $\sim 100\%$ linearly polarized, with a flat polarization position angle across the bursts; no circular polarization is detected (Gajjar et al. 2018; Michilli et al. 2018). This provides new clues about the emission mechanism, and allows a more detailed phenomenological comparison to be made with other known types of millisecond-duration astronomical radio signals —including various forms of pulsar and magnetar pulsed radio emission, which are often highly polarized (e.g., Gould & Lyne 1998; Eatough et al. 2013). The polarized signal also reveals that an extreme Faraday rotation is imparted on the bursts: the rotation measure (RM) in the source frame was $\mathrm{RM}_{\mathrm{src}} = 1.46 \times 10^5\,\mathrm{rad\,m^{-2}}$ at the first epoch of detection, and was 10% lower 7 months later (Gajjar et al. 2018; Michilli et al. 2018). This shows that FRB 121102 is in an extreme and dynamic magneto-ionic environment—e.g., the vicinity of an accreting massive black hole or within a highly magnetized

PWN/MWN and SNR. The properties of the aforementioned persistent radio source are consistent with both these scenarios, as are the constraints from the nondetections of persistent high-energy emission (Chatterjee et al. 2017; Marcote et al. 2017; Scholz et al. 2017; Tendulkar et al. 2017).

Here we present a multifrequency subset of high signal-to-noise FRB 121102 bursts that better demonstrate the complex time–frequency structure hinted at by previously reported bursts in the literature (e.g., Scholz et al. 2016, 2017; Spitler et al. 2016). These add substantial observational clues for modeling the underlying emission mechanism and propagation effects imparted near the source. In Section 2 we present the observations and selection of the burst sample. We analyze the time–frequency properties of this sample in Section 3, and discuss possible consequences for understanding FRB 121102, and the FRBs in general, in Section 4. Lastly, in Section 5 we conclude and provide an outlook to future work inspired by the results presented here.

2. Observations and Burst Sample

2.1. Arecibo and Green Bank Telescope (GBT) Observational Configurations

Until recently, the available time and frequency resolution of FRB detections has been a limitation in studying their properties. Even in the case of real-time detections, dedispersion of the bursts has typically been done incoherently (though see Farah et al. 2018), meaning that there is residual time smearing from intrachannel delays (Petroff et al. 2015a; Keane et al. 2016). The known DM of FRB 121102 allows for coherent dedispersion,[18] and the precise localization allows observations up to much higher frequencies (where the telescope field of view is narrower) compared to all other known FRB sources (Gajjar et al. 2018).

Arecibo observations (project P3094) were performed with the L-Wide receiver, which provides a 1150–1730 MHz band, dual linear polarizations, a gain $G \sim 10.5\,\mathrm{K\,Jy^{-1}}$, and a system temperature $T_{\mathrm{sys}} \sim 30\,\mathrm{K}$. Coherently dedispersed filterbank data with full-Stokes information were recorded using the PUPPI backend (a clone of the GUPPI backend, described in DuPlain et al. 2008). Before each integration on FRB 121102, we also acquired a 60 s calibration scan for polarimetric calibration. The 8 bit data provide 10.24 μs time resolution and 1.5625 MHz spectral channels. These channels were coherently dedispersed online to a fiducial $\mathrm{DM}_{\mathrm{fid}} = 557.0\,\mathrm{pc\,cm^{-3}}$. Hence, any residual intrachannel dispersive smearing is negligible as long as this is close to the true DM of the bursts: for deviations, $\Delta \mathrm{DM}_{\mathrm{fid}}$, from $\mathrm{DM}_{\mathrm{fid}}$ the residual temporal smearing scales as $\sim 4 \times \Delta \mathrm{DM}_{\mathrm{fid}}\,\mu$s—i.e., DM smearing is $\lesssim 20\,\mu$s in these data. For comparison, the intrachannel DM smearing in the original FRB 121102 burst detections made with the Arecibo Mock Spectrometers was 700 μs (Spitler et al. 2014, 2016).

GBT observations (projects GBT16B-391, GBT17A-319) used the S-band receiver, with a 1600–2400 MHz band, dual linear polarizations, a gain $G \sim 2\,\mathrm{K\,Jy^{-1}}$, and a system temperature $T_{\mathrm{sys}} \sim 25\,\mathrm{K}$. Data were recorded with the GUPPI backend (DuPlain et al. 2008) in an identical observing mode, and with the same time/frequency resolutions and polarimetric calibration scans as those described above for Arecibo/PUPPI.

---

[18] A method that completely corrects for intrachannel smearing from dispersive delay; see Hankins & Rickett (1975) and Lorimer & Kramer (2004).

2.2. Selection of Burst Sample

To search the Arecibo coherently dedispersed filterbank data for bursts, we first used `psrfits_subband` from psrfits_utils[19] to subband and downsample the raw data to 12.5 MHz frequency channels and 81.92 μs total intensity (Stokes *I*) time samples. Using the PRESTO[20] (Ransom 2001) tool `prepsubband`, we then created dedispersed time series (summed over the full 800 MHz frequency band), using a range of trial DMs from 461 to 661 pc cm^{-3}, in steps of 1 pc cm^{-3}. The GBT data were processed in a very similar way, but in this case the subbanded data used 40.96 μs time samples and kept the full 1.56 MHz frequency resolution, while the DM trials were for a range of 527–587 pc cm^{-3} and step size 0.1 pc cm^{-3}.

In both cases, the dedispersed time series were searched for single pulses using PRESTO's `single_pulse_search.py`. We chose not to apply a radio frequency interference (RFI) mask in this process in order to avoid the possibility of rejecting a very bright and relatively narrowband burst. The dynamic spectra (radio frequency versus time) of candidate single-pulse events were inspected by eye to differentiate genuine astrophysical bursts from RFI.

The 1.4 GHz Arecibo sample presented here was detected during a high-cadence observing campaign in 2016 September (Chatterjee et al. 2017; Law et al. 2017). Specifically, the sample was selected by choosing bursts with signal-to-noise ratio (S/N) > 60, as reported by `single_pulse_search.py`, which searches a range of pulse widths using a boxcar matched filter. This S/N is calculated after averaging the signal over the full band and corresponds to an equivalent fluence limit of >0.2 Jy ms, assuming a 1 ms wide burst. The S/N threshold was chosen in order to select just the brightest detected bursts, but to also retain a sufficiently large sample. A complementary sample of Arecibo bursts observed at 4.5 GHz, using the identical PUPPI recording setup, is presented in Michilli et al. (2018). We do not include a reanalysis of those bursts here because the available fractional observing bandwidth (~15%) is significantly lower compared to the data presented here, and insufficient to accurately study their broadband spectral behavior (see also the discussion below).

The 2.0 GHz GBT bursts are from 2016 September and 2017 July and were also selected to have S/N > 60 (this corresponds to an equivalent fluence limit of >0.8 Jy ms, assuming a 1 ms wide burst). We chose an identical S/N threshold as for the Arecibo selection, in order to have comparable sensitivity to faint structures in the bursts. To complement the Arecibo and GBT bursts, we also include in the sample a highly structured burst observed over an ultrawide band of 4.6–8.2 GHz with the GBT as part of the Breakthrough Listen (BL) project[21] (for further details of the observational setup and analysis used to detect that burst, see Gajjar et al. 2018).

The full sample considered here is summarized in Table 1 along with, as a point of comparison, the earliest 1.4 GHz FRB 121102 burst detected using coherent dedispersion (Scholz et al. 2016). For each of the selected bursts, we used `dspsr` (van Straten & Bailes 2011) to extract a window of full-resolution, full-Stokes raw data around the nominal burst time and produced a dedispersed dynamic spectrum using tools from PSRCHIVE[22] (van Straten et al. 2012). We then manually excised narrowband RFI (channels with excess power before and/or after the burst), blanked recorded channels beyond the edges of the receiver band, and applied a bandpass correction using tools from PSRCHIVE. The resulting dynamic spectra of the bursts[23] are shown in Figure 1. They reveal a variety of temporal and spectral features, and in the rest of this Letter we will refer to bright, relatively isolated patches in time–frequency as "subbursts." Note that the narrowband, horizontal stripes in these dynamic spectra are due predominantly to RFI excision, which is necessary in order to reveal faint features in the bursts (the exception is GB-BL, where scintillation is also visible). We analyze the time–frequency properties of the bursts and their subbursts in Section 3.

We note that selecting only bursts with large S/Ns possibly introduces a bias toward more complex structure, if this structure is typically faint compared to the brightest peak in a burst. This may contribute to why the bursts in the sample presented here are typically more complex in morphology compared to the entire sample of bursts detected and reported so far (e.g., Scholz et al. 2016; Spitler et al. 2016). However, we also note that high-S/N, relatively unstructured bursts have been detected from FRB 121102 (e.g., Marcote et al. 2017; Scholz et al. 2017), and the subbursts are often of comparable brightness. This suggests that any such bias is not strong.

3. Analysis and Results

Here we present the properties of the burst sample defined in Section 2.

3.1. DM Ambiguities

The dispersive delays across the Arecibo 1.4 GHz and GBT 2.0 GHz bands are roughly 1.0 s and 0.5 s, respectively, for $DM_{fid} = 557$ pc cm^{-3}. The dynamic spectra shown in Figure 1 are corrected using our best estimate of the dispersive delay. However, there is an ambiguity between burst structure and DM because of the evolving burst morphology with radio frequency. For example, a frequency-dependent profile shift on the order of 1 ms can influence the measured DM at the 0.5 pc cm^{-3} level, and this is easily detectable, even by eye. Furthermore, intrinsically frequency-dependent emission time or local propagation effects can also possibly influence the apparent DM. Hence, while a large fraction (>99%) of the frequency-dependent arrival time delay is likely due to dispersion in the intervening Galactic, intergalactic and host galaxy medium, there may also be additional nondispersive effects that are difficult to distinguish from DM.

Before we can analyze the time–frequency properties of the bursts in detail, we must decide on an appropriate metric for determining DM. We argue that choosing a DM that maximizes the peak S/N of the bursts is incorrect in this case. Instead, we search a range of trial DMs and, effectively, we determine at what DM value the subbursts appear dedispersed individually (i.e., the emission in each subburst arrives simultaneously across the band, after correcting for dispersion using this DM). This makes the basic assumption that burst temporal components

---

Table 1
Properties of Detected Bursts

ID[a]	Barycentric Peak Time (MJD)[b]	Peak Flux Density (Jy)[c]	Fluence (Jy ms)[c]	W_{sb} (ms)[d]	W_b (ms)[e]	Drift Rate (MHz ms^{-1})[f]	DM Max. $(dl/dt)^2$ (pc cm^{-3})[g]	DM Peak S/N (pc cm^{-3})[h]
AO-00	57364.2046326656	0.03	0.1	…	…	…	…	557.7(2)
AO-01	57638.4659716231	0.3	0.6	1.03	1.94	−204	…	561.50(2)
AO-02	57638.4675640004	0.4	0.6	0.19	2.50	−122	560.68(2)	562.96(2)
AO-03	57640.4138405217	0.1	0.2	0.25	1.89	−187	…	562.24(2)
AO-04	57641.4594528637	0.2	0.2	0.30	1.52	−221	…	562.24(2)
AO-05	57641.4645632098	1.0	6.2	0.34	5.42	−46	560.60(3)	565.85(2)
AO-06	57642.4715691734	0.2	0.6	0.31	3.28	−129	560.50(2)	562.66(2)
AO-07	57642.4754649610	0.4	1.1	0.24	2.44	−128	560.50(3)	562.83(2)
AO-08	57644.4110709268	0.2	0.3	0.43	2.45	−140	…	562.16(2)
AO-09	57646.4173141213	0.1	0.3	0.20	2.77	−205	…	561.17(5)
AO-10	57646.4278138709	0.4	0.9	0.23	2.51	−50	560.50(3)	562.52(2)
AO-11	57648.4307890113	0.3	0.6	0.14	2.32	∼0	560.55(3)	560.74(2)
AO-12	57648.4581115606	0.2	0.2	0.35	1.58	−168	560.53(3)	561.68(2)
AO-13	57649.4281585259	0.2	0.6	0.17	2.08	−286	560.67(4)	561.38(2)
GB-01	57647.2964919448	0.4	0.5	0.13	2.10	−237	560.79(1)	564.21(4)
GB-02	57649.3337214719	0.2	0.4	0.16	1.97	−251	560.65(1)	563.96(4)
GB-03	57927.5700691158	0.05	0.1	0.30	2.67	−141	560.5(1)	567.27(8)
GB-04	57928.7263586936	0.05	0.1	0.40	1.95	−276	560.1(1)	563.10(7)
GB-BL	57991.5765740056	0.4	0.5	0.13	1.97	−865	563.86(5)	595.1(4)

Notes. Uncertainties are the 68% confidence interval, unless otherwise stated.
[a] Central observing frequencies: AO-00 to AO-13: 1.4 GHz; GB-01 to GB-04: 2.0 GHz; GB-BL: 6.5 GHz.
[b] Arrival time of the centroid of the full-burst envelope, corrected to the solar system barycenter and referenced to infinite frequency (i.e., the time delay due to dispersion is removed) using an assumed DM = 560.5 pc cm^{-3}.
[c] Uncertainties on peak flux density and fluence are roughly 50% fractional.
[d] The characteristic subburst durations determined from the ACF analysis. Uncertainties are on the order of 50 μs.
[e] The characteristic burst durations determined from the ACF analysis. Uncertainties are on the order of 50 μs.
[f] Best-fit linear trend to the subburst centroids. A negative sign is used to indicate decreasing frequency. Uncertainties are not well quantified, but it is clear that a simple linear fit is a poor model in some cases.
[g] DM at which the squared time derivative of the profile is maximized.
[h] DM at which the peak S/N is maximized.

each emit simultaneously over a broad range of frequencies; a different underlying assumption, e.g., that there is an intrinsic, frequency-dependent delay in emission time, could also be considered. Furthermore, here we determine a single DM per burst, and do not attempt to find separate DMs for individual subbursts (these could have different apparent DMs in certain scenarios, as we discuss below).

To find an optimal DM under these assumptions, we maximize the steepness, i.e., time derivative, of peaks in the frequency-averaged burst profile. Specifically, we search for the DM that maximizes the mean square of each profile's forward difference time derivative.[24] Because these time derivatives are susceptible to noise, and because we are searching for features that vary with DM, a two-dimensional Gaussian convolution (with $\sigma_{DM} = 0.08$ pc cm^{-3} and $\sigma_{time} = 82$ μs) is performed within the DM versus time space before squaring and averaging over the time axis. The resulting mean squared versus DM curve is then fitted with a high-order polynomial, and the peak DM value is then interpolated from this fit (Figure 2).

This is roughly the same as maximizing the structure in the frequency-averaged burst profile. We find that all the 1.4 GHz and 2.0 GHz bursts in this sample are well modeled by a DM ∼ 560.5 pc cm^{-3} (Table 1). In contrast, maximizing the peak S/N of each burst leads to subbursts that overlap in time and sweep upward in frequency, as well as displaying a broader

range of apparent DMs (see also Figure 1 of Gajjar et al. 2018). The AO-01 to AO-13 bursts span a time range of only 11 days, and for 8 of these it was possible to derive a structure-maximizing DM (for the others, the method did not converge). The average DM of these bursts is 560.57 pc cm^{-3}, with a standard deviation of 0.07 pc cm^{-3}—comparable to the formal uncertainties on the individual DM determinations. Given how well a single DM per burst aligns the subbursts such that each arrives at a consistent time across the frequency band (post dedispersion), we estimate that variations in apparent DM between subbursts are ≲0.1 pc cm^{-3}. In contrast, for these same eight bursts, the DMs from maximizing peak S/N are systematically higher, with an average of 562.58 pc cm^{-3} and a much larger standard deviation of 1.4 pc cm^{-3}. The much smaller scatter in DMs from the structure-maximizing metric arguably further justifies that approach; however, given the extreme magneto-ionic environment of the source (Michilli et al. 2018), we cannot rule out that there are relatively large DM variations between bursts.

3.2. DM Variability

The complex and frequency-dependent burst profiles show that adequate time resolution is critical in determining accurate DMs for FRB 121102 and, by extension, whether DM varies with epoch. A DM = 560.57 ± 0.07 pc cm^{-3} at MJD 57,644 (the average epoch of bursts AO-01 to AO-13) is roughly compatible with the range DM = 558.1 ± 3.3 pc cm^{-3} found by Spitler et al. (2016)—i.e., the earliest sample of detected
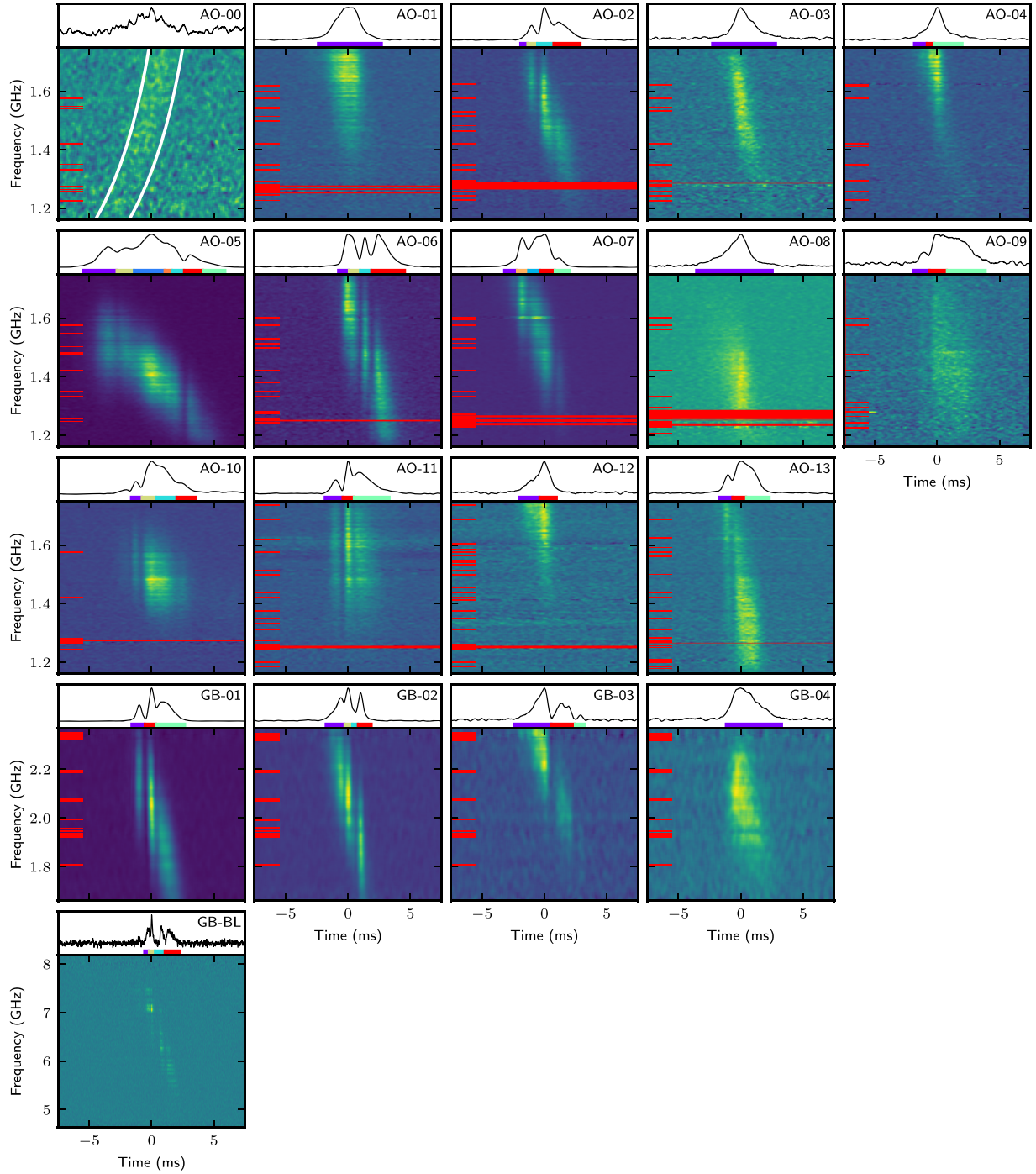
---
[24] For a similar approach, see Gajjar et al. (2018).

Figure 1. Dynamic spectra of the bursts (see Table 1), each dedispersed to DM = 560.5 pc cm^{-3}, and using a linear scaling in arbitrary units (the bursts are not flux calibrated). The plotted dynamic spectra have been smoothed using a Savitzky–Golay filter (Savitzky & Golay 1964), which preserves higher moments of the peak while providing a natural way to interpolate across modest gaps in the data due to RFI excision (indicated with red tick marks on the left). Larger gaps are indicated with full red bars. The smoothing time and frequency scales are AO-00: 0.5 ms/25 MHz, AO-01–13: 0.5 ms/8 MHz, GB-01–04: 0.5 ms/55 MHz, and GB-BL: 0.05 ms/60 MHz. At the top of each panel, the band-integrated burst profile is shown, with the colored bars indicating the time spans of the subbursts used in the fitting. Bursts AO-01 to AO-13 are the new bursts detected with Arecibo. For comparison, AO-00 is burst #17 from Scholz et al. (2016); the white lines show the best-fit DM = 559 pc cm^{-3} for that burst, which deviates significantly from the DM = 560.5 pc cm^{-3} dispersive correction displayed here. GB-01 to GB-04 are the four new GBT bursts detected at 2.0 GHz, and GB-BL is one of the 6.5 GHz GBT Breakthrough Listen bursts presented in Gajjar et al. (2018).

bursts from MJD 57,159 and MJD 57,175. However, those data were only incoherently dedispersed, and hence unresolved burst structure may be the cause of the apparent spread in DMs in the Spitler et al. (2016) sample. Furthermore, those DMs were determined using an S/N-maximizing metric, and hence are overestimated if there was unresolved, frequency-

dependent subburst structure like that seen in the sample presented here.

In the upper left panel of Figure 1, we show the dynamic spectrum of AO-00, the earliest 1.4 GHz burst from FRB 121102 detected using coherent dedispersion (first presented as "burst 17" in Scholz et al. 2016), as it appears dedispersed to 560.5 pc cm^{-3}. The optimal DM value for
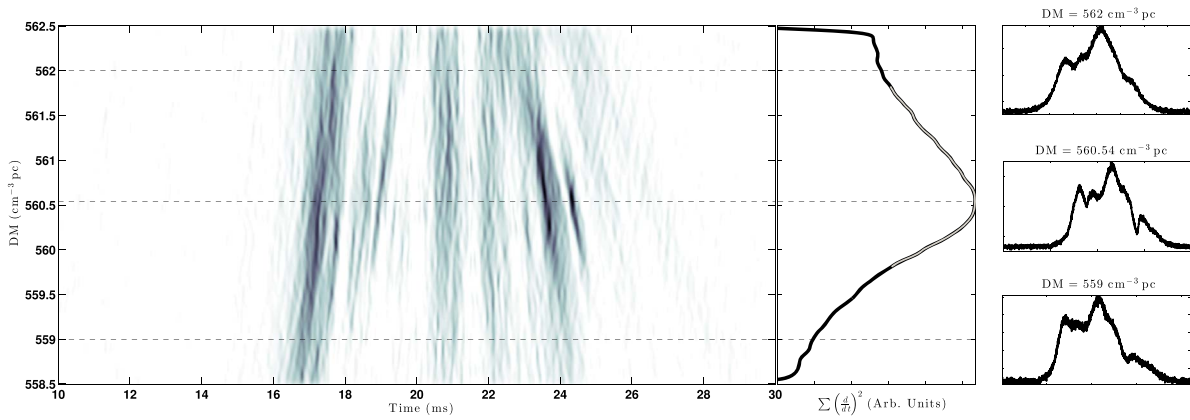
Figure 2. Example of the DM optimization method, using burst AO-05. The main panel presents the square of the Gaussian-smoothed forward difference time derivative of the frequency-averaged burst profile as a function of DM and time. Darker regions show steeper areas of the profile when varying DM. The adjacent subpanel shows the average along the time axis. Here the gray curve overlaid on the time-average curve is the high-order polynomial used for the optimal DM interpolation. The right-hand panels show the frequency-averaged burst profiles at DM values above, at, and below the optimum value, which are marked with dashed lines in the main panel.

MJD 57,644 appears to be slightly too high for this burst from MJD 57,364, where Scholz et al. (2016) found the optimal value to be $558.6 \pm 0.3 \pm 1.4 \, \mathrm{pc \, cm^{-3}}$. This value optimizes both peak S/N and burst structure; here the quoted uncertainties are, in order, statistical and systematic, where the systematic uncertainty was based on measuring the ΔDM that results in a DM delay across the band equal to half the burst width. However, because this burst was coherently dedispersed, we argue that it is unnecessary to consider this additional systematic uncertainty, which was added to account for possible frequency-dependent profile evolution. In summary, comparing the burst DMs in the sample here with those of the earliest detections suggests that the DM of FRB 121102 has increased by $\sim$1–3 pc cm^{-3} ($\sim$0.2%–0.5% fractional) in the 4 yr since its discovery, but we caution that there could be stochastic variations on shorter timescales and that this is not necessarily a secular trend.

3.3. Polarimetry

The recent detection of FRB 121102 bursts at relatively high radio frequencies (4–8 GHz; Gajjar et al. 2017, 2018; Michilli et al. 2018; Spitler et al. 2018) has enabled the detection of a high linear polarization fraction ($L/I \sim 100\%$), no detectable circular polarization ($|V|/I \sim 0\%$), and an exceptionally large Faraday RM ($\mathrm{RM_{src}} = 1.46 \times 10^5 \, \mathrm{rad \, m^{-2}}$). Bandwidth smearing (intrachannel phase wrapping) in the 1.5 MHz channels at frequencies <2.4 GHz explains why previous polarization searches have been unsuccessful, if the observer frame RM was $\gtrsim 10^5 \, \mathrm{rad \, m^{-2}}$ at those epochs. Additionally, it is possible that FRB 121102 is less polarized at lower frequencies. For the 1.4 and 2.0 GHz bursts presented here, we nonetheless searched for polarized emission using PSRCHIVE's `rmfit` routine to investigate a range $|\mathrm{RM}| < 3 \times 10^5 \, \mathrm{rad \, m^{-2}}$ after a basic polarimetric calibration (see Michilli et al. 2018, for details). This was to check whether the RM was perhaps much lower at earlier epochs, but again no linearly or circularly polarized emission was detected above a 3σ significance. The polarimetric properties of the high-frequency burst GB-BL (Table 1, Figure 1) are presented in Gajjar et al. (2018).

3.4. Time–Frequency Burst Analysis

As can be seen in Figure 1, the burst sample displays a significantly more complex structure than previously reported bursts from FRB 121102, most of which appeared single peaked (Scholz et al. 2016, 2017; Spitler et al. 2016; Gajjar et al. 2018; Michilli et al. 2018). In the sample here, bursts show as many as seven components that can be isolated in time and frequency, and which we refer to as subbursts. The subburst separations are $\sim$1 ms, and hence are much more closely spaced compared to the shortest published burst separations to date: $\sim$40 ms (Scholz et al. 2017) and 34 ms (Hardy et al. 2017). Though there is typically a gradual rise into the first subburst, it often appears that the leading edges of subsequent subbursts show a sharper rise in brightness compared to the more gradual decay in the trailing edges. Shorter-timescale subburst structure is sometimes seen on top of wider, more diffuse emission. Between subbursts, there are sometimes sharp drops in brightness. The overall time–frequency structure is reminiscent of a diffraction pattern, showing isolated peaks and troughs in brightness. There is no obvious similarity in the time–frequency structures of bursts detected within a single observation, or even for bursts separated by only a few minutes in time. Of the bursts presented here, the shortest and longest separations between bursts observed within the same observing session are $\sim$138 s for bursts AO-01 and AO-02 and $\sim$2360 s for bursts AO-11 and AO-12, respectively (Table 1). In the following, we quantitatively characterize the burst features.

First, we manually identified individual subbursts, whose time spans are indicated by colored bars under the frequency-averaged profiles in Figure 1. This is an imperfect time division of the bursts because some subbursts are less distinct than others, and because there is sometimes also more diffuse underlying emission. We used a least-squares fitting routine (Levenberg–Marquardt algorithm) to measure the characteristic bandwidth and duration of each subburst using a 2D Gaussian function. These Gaussians were aligned along the time and frequency axes, and thus we did not fit for any residual time–frequency drift within subbursts. This is because any such analysis is additionally complicated by frequency evolution of the subburst profiles. Also, we note that this fitting is not significantly influenced by RFI excision, which only affects the
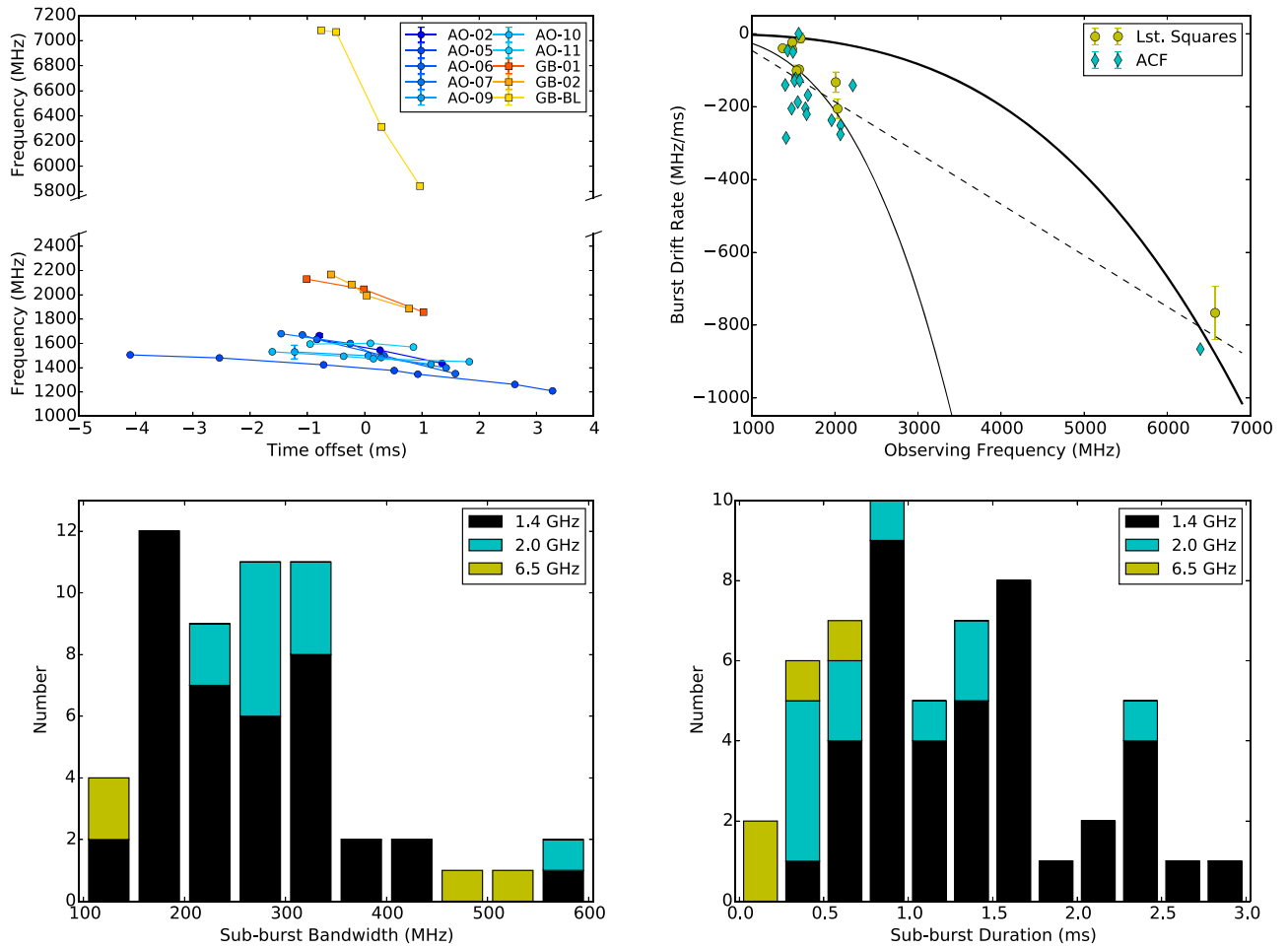
6

Figure 3. Top left: subburst central frequency as a function of arrival time. The bursts are aligned such that, for each burst, emission at the average frequency of the subbursts arrives at zero time offset. This is to demonstrate that they have similar slopes at the same central observing frequency. Top right: measured linear burst drift rates vs. burst characteristic radio frequency for the least-squares (yellow circles) and ACF (cyan diamonds) methods. The solid curves illustrate the drift expected if the DM used to dedisperse the burst was too low. The thicker solid line corresponds to a ΔDM ~ 40 pc cm^{-3} as determined through a least-squares fit to all of the data points, while the thinner solid line corresponds to ΔDM ~ 5 pc cm^{-3} as determined through a least-squares fit to only the 1.4 and 2.0 GHz bursts. The dashed line illustrates a linear fit to the data. Bottom left: the FWHM bandwidths measured by fitting a 2D Gaussian model to each subburst in the sample using the least-squares routine. The 1.4 GHz Arecibo bursts are shown in black, the 2.0 GHz GBT bursts in cyan, and the 6.5 GHz GBT bursts in yellow. Bottom right: the 2D Gaussian FWHM temporal durations of each subburst as determined by the least-squares fitting technique. Color coding is the same as for the bottom left panel.

spectrum on a much narrower frequency scale compared to the bandwidths of the subbursts.

Figure 3 shows the distribution of subburst bandwidths and durations for the 1.4, 2.0, and 6.5 GHz bursts. For the 1.4 GHz bursts, we find that the subbursts emit with a characteristic bandwidth of $\sim$250 MHz, although with a 1σ variation of $\sim$90 MHz. For the few 2.0 and 6.5 GHz bursts included in this sample, the characteristic bandwidth is comparable, but somewhat higher on average. Note that the $\sim$100 MHz features seen in the GB-BL 6.5 GHz subbursts are consistent with originating from Galactic diffractive interstellar scintilliation (DISS; Gajjar et al. 2018).

Overall burst durations at 1.4 GHz—defined as the FWHM of the full-burst envelope—are typically $\sim$3 ms and consistent with previous measurements in the literature (e.g., Scholz et al. 2016; Spitler et al. 2016). However, most bursts show narrower internal structure (subbursts) with widths $\lesssim$1 ms. Note that these subbursts are resolved in time and are not significantly affected by intrachannel dispersive smearing or interstellar scattering (see Section 3.5).

Burst durations at 2.0, 4.5, and 6.5 GHz appear to be systematically smaller than at 1.4 GHz (see also Figure 7 of Gajjar et al. 2018). For example, Michilli et al. (2018) found total burst durations of $\lesssim$1 ms for their sample of bursts detected at 4.5 GHz. However, the sample sizes are small and this trend requires confirmation. Also, these multifrequency bursts were observed at different epochs, and it is possible that burst width also changes with time, systematically.

To complement the 2D Gaussian least-squares fitting of individual subbursts (which were first manually identified to provide initial parameters to the fit), we also performed an unguided 2D autocorrelation function (ACF) analysis (Figure 4) of the dedispersed dynamic spectra of the bursts. The characteristic subburst durations (W_{sb} in Table 1) are from this analysis.

Particularly striking is the tendency for the characteristic frequency of the subbursts (i.e., the central frequency of a band-limited subburst) to drift to lower frequencies at later times during the burst. We characterized this drift using both fitting methods. For the least-squares technique, the centers of the best-fit 2D Gaussians in frequency and time for each burst (Figure 3, top left) were fit to a linear model. Only bursts with three or more components and with frequency centers within the band were included. The resulting slopes are shown in
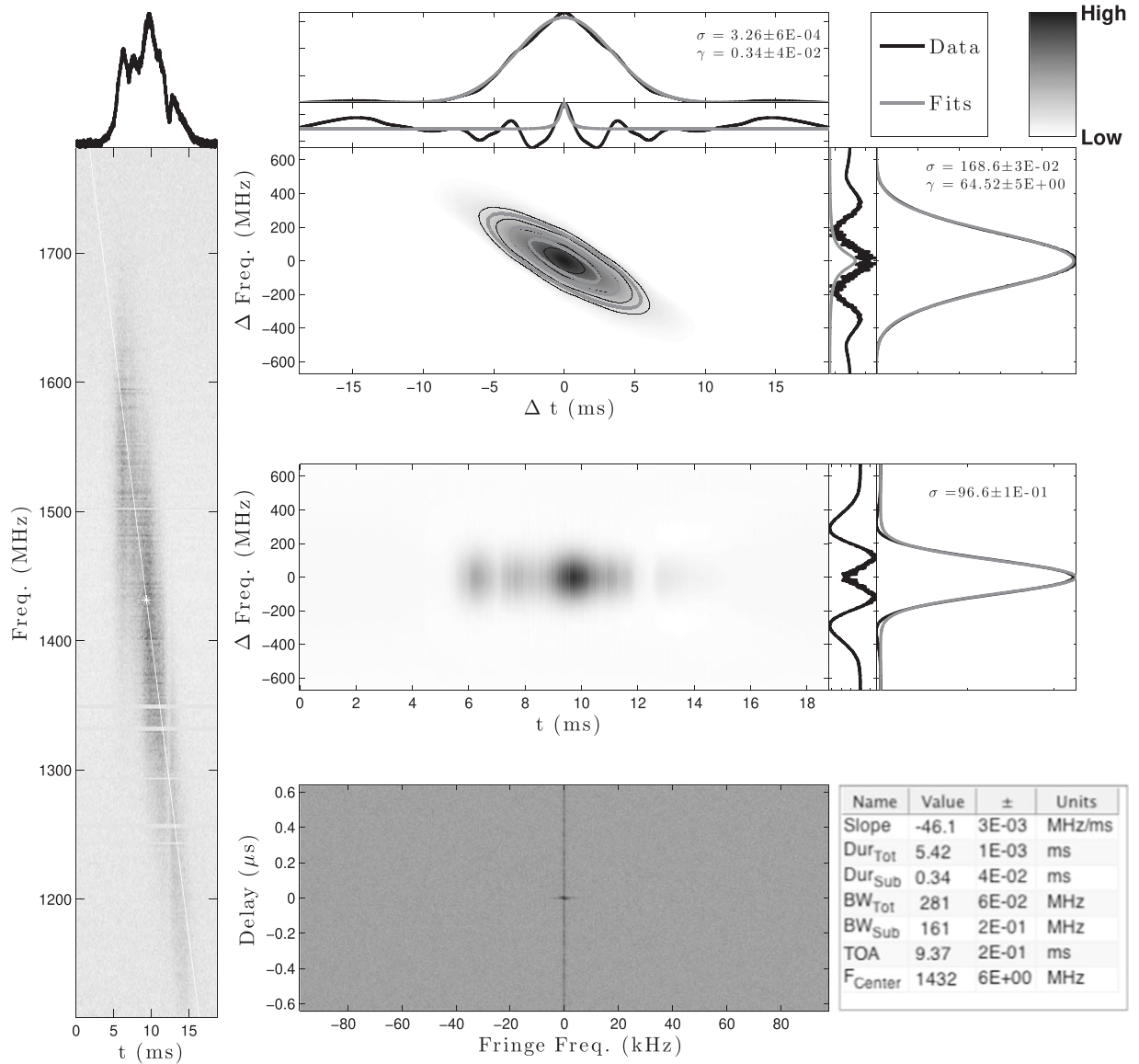
Figure 4. Diagnostic plot from the autocorrelation function (ACF) burst analysis, using burst AO-05 as an example. Left: the dynamic spectrum, with the profile averaged over frequency shown above. Here the white diagonal line and star show the fitted drift and characteristic frequency of the burst. Top right: a two-dimensional ACF for the burst, with adjacent subpanels showing the average along each axis. These average ACF curves are fitted with a Gaussian distribution, and the residuals of those are fitted with a Lorentz distribution. Center right: the nonnormalized ACF at each time stamp, with the time-averaged ACF shown in the adjacent subpanel. This time-averaged ACF is fitted with a Gaussian, whose residual is displayed. Bottom right: the secondary spectrum and a table of fitted values.

Figure 3 (top right, yellow circles). Drift rates were also estimated using the ACF method and are listed in Table 1 and shown in Figure 3 (top right, cyan diamonds). Note that the ACF method has the advantage that it can be applied to all bursts, regardless of their number of components. The inferred ACF drift rates are in good agreement with those derived by fitting the central times and frequencies of individual subbursts.

Interestingly, the drift rates of this burst sample are always negative (subbursts peak in brightness at lower frequencies at later times), and the magnitude of the drift rate increases with increasing radio frequency. In one case, however, AO-05 (Figure 1), the first two subbursts show no drift with respect to each other, and only thereafter does the downward trend begin.

The metric that is used to determine DM is a crucial consideration in interpreting these drifts (see Section 3.1); we would also find a drift to lower frequencies at later times if we were under-dedispersing the bursts: $d\nu/dt \propto -\nu^3/\delta\mathrm{DM}$, where

$\delta\mathrm{DM}$ is the residual DM. We calculated the best-fit $\delta\mathrm{DM}$ to the estimated drift rates with the GB-BL burst ($\delta\mathrm{DM} \sim 5\,\mathrm{pc\,cm^{-3}}$) and without the GB-BL burst ($\delta\mathrm{DM} \sim 40\,\mathrm{pc\,cm^{-3}}$). These fits are shown in Figure 3 as the thick and thin solid lines. Clearly, no single value of $\delta\mathrm{DM}$ fits the measurements at all three observing frequencies, and we argue that the drift rate is not caused by residual dispersion. Finally, we fit a line to the rates, and while it is a good fit, the absence of bursts in our sample between $\sim$2 and 6 GHz makes any conclusive statement difficult. Note that the 4.5 GHz bursts presented by Michilli et al. (2018) do not show any clear examples of subburst drift to include in the analysis here. For that sample, the observing bandwidth of 800 MHz is comparable to the $\sim$500 MHz ms^{-1} drift rate that we would predict based on the sample presented here. In fact, the clear drift visible in the 6.5 GHz GB-BL burst presented here is only visible because of the very large bandwidth of those observations.
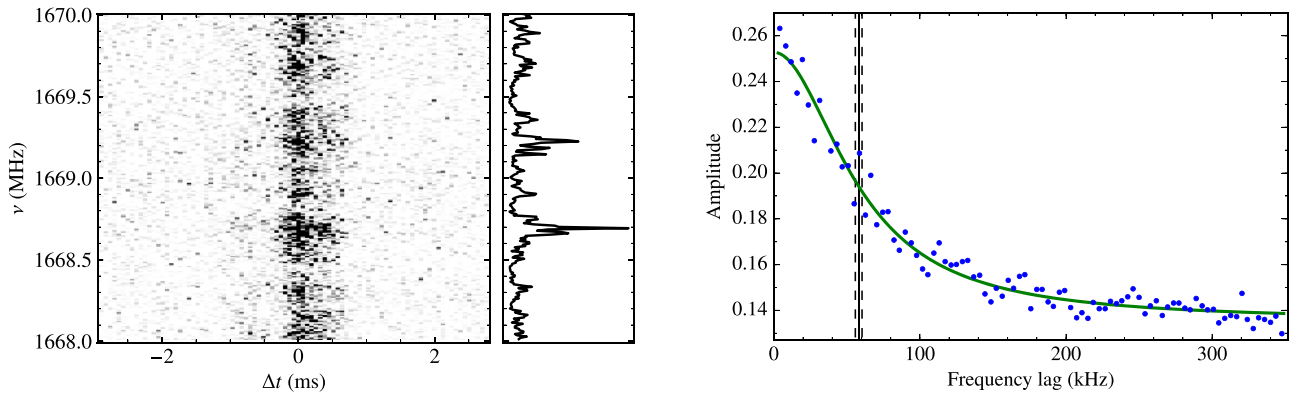
Figure 5. Left: a zoom-in on 2 MHz of the dedispersed dynamic spectrum of a burst detected in European VLBI Network (EVN) observations. The right-hand subpanel shows the cumulative burst brightness (arbitrary units) as a function of frequency. Right: autocorrelation function of the burst spectrum showing that its narrowband frequency structure has a characteristic scale (half width at half maximum, HWHM) of 58.1 ± 2.3 kHz. Here the solid vertical line shows the HWHM of the fitted Lorentzian function (shown by the solid green curve), and the dashed lines show the uncertainty.

3.5. Scintillation

We argue here that Galactic DISS accounts for fine structure in the spectra of the bursts but not for the relatively broadband ($\sim$100–400 MHz) frequency structure observed in the 1.4 and 2.0 GHz subbursts.

To demonstrate this, we reanalyze the brightest European VLBI Network (EVN) burst presented by Marcote et al. (2017), using just the autocorrelations from Arecibo. These voltage data provide only 64 MHz of spectral coverage, but offer the opportunity for much better frequency resolution compared to the PUPPI/GUPPI data available for the other bursts. The EVN burst shows that there is fine-scale frequency structure ($<$MHz) in the total intensity (Figure 5). In principle the structure could be due to DISS exclusively, or a combination between DISS and "self-noise" in the signal. Burst electric fields are well described as an intrinsic shot-noise process modulated by an envelope function. The resulting spectrum has frequency structure with widths equal to the reciprocal burst width; this structure may then combine with the extrinsically imposed scintillation modulation (Cordes et al. 2004). For millisecond bursts like those from FRB 121102 the self-noise frequency structure is on a much different scale compared to the subburst spectral peaks displayed in Figure 1.

To measure a characteristic bandwidth for these narrowband spectral features, we used an ACF analysis (Cordes et al. 1985). We computed the ACFs from power spectral densities generated with a resolution of 3.9 kHz from the dedispersed EVN Arecibo voltage data using only the time range that coincides with the burst. We fitted a Lorentzian function to the ACF using a least-squares approach as implemented in the Levenberg–Marquardt algorithm. The central lag of the ACF, which is dominated by noise, was excluded from the fit. Furthermore, because of bandpass effects, only the central 80% of the frequency range in each of the four subbands was used to compute the ACF. We measure a characteristic bandwidth of 58.1 ± 2.3 kHz at 1.65 GHz, which corresponds to the half width at half maximum (HWHM) of the fitted Lorentzian function (Figure 5).

The characteristic bandwidth is consistent to better than a factor of two with the NE2001 Galactic electron model prediction for the DISS contribution from the Milky Way in this direction (Cordes & Lazio 2002): Scaling the model prediction to 1.65 GHz using ν^4 and $\nu^{4.4}$, respectively, yields bandwidths of 87 and 107 kHz. We note that the YMW16

model (Yao et al. 2017) underpredicts the DISS bandwidth by a factor of 30 (1.5 kHz at 1.65 GHz); this will be discussed in a separate paper.

The pulse broadening time at 1.65 GHz corresponding to the DISS bandwidth is $(2\pi \times 58.1 \text{ kHz})^{-1} = 2.7\ \mu$s, which is much smaller than the time resolution of our data. The scintillation timescale is unmeasurable because it is expected to be much larger (order of hours) than the burst durations.

We thus conclude that the narrow ($<$MHz) frequency structures seen in the bursts are due to DISS imparted when they enter the Galaxy, and consequently that the broad ($\sim$100–400 MHz) spectral features and the temporal structure seen in Figure 1 must either be intrinsic or imparted in the local environment of the source (or perhaps elsewhere in FRB 121102's host galaxy).

Similarly, at higher frequencies of 4–8 GHz, Gajjar et al. (2018) and Spitler et al. (2018) found 5–100 MHz frequency structure, which they attributed to Galactic DISS, and which is also consistent with NE2001 predictions. This implies that the $\sim$1 GHz frequency structure in the 6.5 GHz GB-BL burst presented here is also likely intrinsic or imparted near the source.

4. Discussion

4.1. Comparison of FRB 121102 with Other FRBs

FRB 121102 differs notably from other FRBs in the fact that it repeats in an easily detectable way (Spitler et al. 2016). The bursts also display an extreme Faraday rotation (Michilli et al. 2018) that has not been seen in any other FRB to date (see Figure 5 in Caleb et al. 2018, which summarizes all available measurements). While some FRBs have a reasonably high absolute RM ($|\text{RM}| \sim 200$ rad m^{-2}) that originates close to the source (e.g., Masui et al. 2015), others show a very low absolute RM ($|\text{RM}| \lesssim 10$ rad m^{-2}, e.g., Ravi et al. 2016). However, previous polarimetric FRB detections lacked sufficient frequency resolution to resolve such a large RM as seen in FRB 121102, and hence some FRBs with no apparent linear polarization may have very large RMs as well (Petroff et al. 2015a).

Despite the possibility that FRB 121102 has a fundamentally different origin (or inhabits a markedly different environment) compared to the apparently nonrepeating FRBs, it is nonetheless useful to compare its burst structure to what has been

seen in other FRBs. The repeating nature and localization of FRB 121102 have allowed higher time- and frequency-resolution data to be acquired over a relatively large range of frequencies. As such, the detailed time–frequency features it displays may foreshadow what other FRBs will show in similar observations.

While FRB 121102 bursts can clearly be multipeaked, the majority of nonrepeating FRB bursts detected to date appear simple in form. However, in some cases this may simply be because they are broadened by uncorrected intrachannel dispersion smearing (Ravi 2019) or by scattering (Thornton et al. 2013)—either of which can mask submillisecond temporal structure. The multicomponent FRB 121002 and FRB 130729 show time–frequency structures similar to those of FRB 121102 albeit at lower S/N (Champion et al. 2016), though the unknown position of these bursts with respect to the telescope sensitivity pattern makes it difficult to interpret their spectra.

More recently, Farah et al. (2018) present the UTMOST discovery of FRB 170827 at a central observing frequency of 835 MHz. Three temporal components, one only $\sim$30 μs wide, were detected in FRB 170827's burst profile thanks to real-time triggering of voltage data, which allowed coherent dedispersion. With the coarser time sampling, and incoherent dedispersion used to discover this source, this same burst looks similar to the single-component FRBs detected with Parkes (Petroff et al. 2016). This suggests that other high-S/N FRBs analyzed with coherent dedispersion will also show complex temporal structure. The narrow bandwidth (31 MHz) available in the detection of FRB 170827 limits the ability to see whether its subbursts drift in frequency like FRB 121102. The data also do not allow for an RM measurement. Regardless, the burst time structure and timescales are similar to those of FRB 121102. One can thus speculate that, despite FRB 170827's apparent nonrepeatability (Farah et al. 2018), this suggests a similar physical origin to FRB 121102. Ultimately, however, additional observational clues, like host environment and multiwavelength counterparts, are needed to address the question of whether there are multiple FRB progenitor classes or not.

4.2. Comparison with Radio Emission from Neutron Stars

Based on light-travel-time arguments, the short durations of FRB pulses require compact emission regions. For example, the 30 μs wide component detected in one FRB 121102 pulse requires an emitting region $\lesssim$10 km, assuming no additional geometric or relativistic effects (Michilli et al. 2018). Thus it is natural to compare FRB emission to neutron star radio emission, even though FRB 121102 has thus far shown no clear periodicity in its burst arrival times (Spitler et al. 2016; Zhang et al. 2018). Like FRB 121102, pulsars and magnetars show a wide range of pulse complexity in the time domain. In the case of pulsars, this results from the rotation of fluctuating beamed radiation across the line of sight. FRB 121102 differs markedly from pulsars and magnetars in several ways, however; in particular, its bursts are enormously more energetic. Both pulsar pulses and FRBs have peak flux densities $\sim$1 Jy but the $\sim$$10^6$ times greater distance of FRB 121102 implies a $\sim$$10^{12}$ times greater luminosity (for equal solid angles).

Pulsar-type magnetospheres may have difficulty providing this energy (e.g., Cordes & Wasserman 2016; Lyutikov 2017).

Alternatively, bursts from FRB 121102 may be powered by the strong $\sim$$10^{14}$–$10^{15}$ G magnetic fields in magnetars (Popov & Postnov 2013; Beloborodov 2017).

Another marked difference between FRB 121102 and typical pulsars and radio-emitting magnetars is in the spectral domain, where the latter objects have smooth, wide-band spectra (even in their single pulses, e.g., Kramer et al. 2003; Jankowski et al. 2018) whose only narrowband modulation is from DISS, augmented in some cases by constructive and destructive interference from multiple imaging by interstellar refraction. While the radio-emitting magnetars have shown variable spectra, these remain well fit by a broadband power law (e.g., Lazaridis et al. 2008). In contrast, the confinement of FRB 121102 bursts to frequency bands of width $\sim$250 MHz (at $\sim$1.4 GHz) is different compared to variable magnetar spectra, and also cannot be explained by Galactic DISS. To our knowledge, no similar effect is seen in pulsars except for the high-frequency interpulse of the Crab pulsar, or in cases of plasma lensing (which we will discuss in the following subsection).

Indeed, the giant pulse emission in the Crab pulsar's high-frequency interpulse (HFIP; Hankins et al. 2016), seen at radio frequencies above $\sim$4 GHz, provides an intriguing observational analogy. Notably, the properties of the HFIPs differ significantly from those of the main giant pulses (MP; Jessner et al. 2010; Hankins et al. 2016). Since the Crab is a young ($\sim$1000 yr old) neutron star embedded in a luminous nebula, it is also an interesting Galactic example of the young PWN/SNR scenario for FRB 121102. It is possible that the FRB 121102 system is simply a much younger version of the Crab, though understanding the scaling to the energies required by FRB 121102 remains challenging. A highly focused beam, or intrinsically narrowband emission can reduce the required energy.

The Crab's HFIP spectra exhibit periodic banded structure (Hankins & Eilek 2007) with separations $\Delta\nu$ that scale with frequency ($\Delta\nu/\nu$ = constant). Drift rates in FRB 121102 may show a similar scaling (Figure 3) but there are too few bursts in our sample to be conclusive. Furthermore, we note that while the Crab HFIPs are microseconds in duration, the burst envelopes of FRB 121102 are typically milliseconds—though with underlying $\sim$30 μs structure clearly visible in some cases (Michilli et al. 2018). Searches for even finer-timescale structure in FRB 121102 should continue, using high observing frequencies to avoid smearing from scattering.

The polarization angle of the $\sim$100% linearly polarized radiation from FRB 121102 at 4–8 GHz appears constant across bursts and is stable between bursts (Gajjar et al. 2018; Michilli et al. 2018). Here again there is phenomenological similarity with the Crab's HFIPs, which are $\sim$80%–100% linearly polarized with a constant polarization position angle across the duration of each pulse and also between HFIPs that span $\sim$3% of the pulsar's rotational phase (see Figure 14 of Hankins et al. 2016). Like FRB 121102, the Crab HFIPs typically also show no circular polarization.

4.3. Intrinsic Processes and Propagation Effects

The spectral properties of FRB 121102 may be intrinsic to the radiation process, post-emission propagation processes, or some combination of the two.

Spectral structure is seen in bursts from the Sun (e.g., Kaneda et al. 2015), flare stars (e.g., Osten &

Bastian 2006, 2008), and solar system planets (e.g., Zarka 1992; Ryabov et al. 2014), including auroral kilometric radiation from the Earth and Saturn and the decametric radiation from Jupiter (e.g., Treumann 2006). Frequency drifts, qualitatively similar to those seen from FRB 121102, occur due to upward motions of emission regions to locations with smaller plasma frequencies or cyclotron frequencies, which are tied to the observed electromagnetic frequency. Fine structure in the emission is related to structure in the particle density (e.g., Treumann 2006). Extrapolation of similar processes to FRBs suggests that FRB 121102's emission could originate from cyclotron or synchrotron maser emission (Lyubarsky 2014; Beloborodov 2017; Waxman 2017), in which case relatively narrowband emission in the gigahertz range could be expected. Antenna mechanisms involving curvature radiation from charge bunches have also been considered (Cordes & Wasserman 2016; Lu & Kumar 2018) but it is not clear if the energetics can be satisfied or how time–frequency structure is produced.

Alternatively, burst propagation through media outside the emission region can also produce spectral features by refraction and diffraction from large- and small-scale structure in ionized plasma, respectively. Enhanced electron densities in confined regions can act as diverging (overdensities) or converging (underdensities) lenses—i.e., "plasma lenses." The resulting effects produce highly chromatic amplifications and multiple images (Clegg et al. 1998; Bannister et al. 2016; Cordes et al. 2017; Main et al. 2018) with bandwidths strongly dependent on the detailed properties of the lenses. Multiple images of bursts will have different amplitudes, peak frequencies, arrival times, and DMs. If burst images overlap in time and frequency, they can produce interference structure on small time and frequency scales, including oscillations that follow the square of an Airy function (Watson & Melrose 2006; Cordes et al. 2017). This is qualitatively similar to what we observe from FRB 121102, and though we can model individual bursts well with a single DM, small differences ($\lesssim 0.1 \, \mathrm{pc \, cm^{-3}}$) in DM between subbursts may still be present, allowing for the possibility of different bursts being slightly differently lensed.

Michilli et al. (2018) argue that FRB 121102 is embedded in a compact, ionized region with a magnetic field of at least a few milli-Gauss and a substantial electron density ($n_e \gtrsim 10 \, \mathrm{cm^{-3}}$). The large RM suggests that the ionized gas is dominated by a nonrelativistic Hydrogen–Helium plasma because a relativistic gas or gas comprising an electron-positron plasma would yield a small or null RM.

The large variation in RM between bursts separated by 7 months—without a similarly large accompanying DM variation—indicates that the region is dynamic, possibly much smaller than 1 pc in thickness, and contains even smaller ~astronomical-unit-size structures that could cause plasma lensing. Depending on the ratio of thermal to magnetic pressure in the plasma, β, and the geometry of the field (disordered or misaligned from the line of sight), the requirements for plasma lensing give a consistent picture for the measured RM if the region's depth is of order ~au, the electron density ~$10^4 \, \mathrm{cm^{-3}}$ and the field $\gtrsim 1 \, \mathrm{mG}$. Note that the magnetic field strength could even be a thousand times larger, ~1 G, if the DM related to the Faraday region is small ($\lesssim 1 \, \mathrm{pc \, cm^{-3}}$).

The detection of transient pulse echoes from the Crab pulsar presents an observational precedent for plasma lensing (Graham Smith et al. 2011). While these echoes are fainter

than the normal Crab pulsar emission, the possibility that FRB 121102 is also embedded in a dense nebula suggests an interesting analogy. Though such large RMs as seen from FRB 121102 have not been observed in the Crab pulses, the Crab echo events are associated with apparent DM variations[25] of ~0.1 pc cm^{-3} (Backer et al. 2000), which are similar but less extreme compared to the order ~1 pc cm^{-3} variations seen in FRB 121102.

More recently, Main et al. (2018) discovered that plasma lensing can boost the observed brightness of the "black widow" Galactic millisecond pulsar PSR B1957+20 in a strongly time and frequency-dependent way.[26] PSR B1957+20 is a binary millisecond pulsar, which is eclipsed by intrabinary material blown off of the companion star by the pulsar wind. The plasma lensing events occur near eclipse ingress and egress, and last for a few to tens of milliseconds. Their dynamic spectra (see Figure 2 of Main et al. 2018) are qualitatively similar to those of FRB 121102 presented here. While this is a stunning demonstration of how plasma lensing can boost the observed brightness of pulsed radio emission by close to two orders of magnitude, we note that FRB 121102 likely inhabits a much different environment compared with PSR B1957+20 (Michilli et al. 2018).

Furthermore, while plasma lensing can explain the downward frequency drift of the FRB 121102 subpulses, this would require a single dominant lens for the drift to be in the same direction for some amount of time. If plasma lensing is the cause for the subburst frequency drift, one would expect the drift rate to change rate and sign with time, as the viewing geometry changes and different lenses dominate. In the case of PSR B1957+20, where many lenses are involved, brightness enhancements are seen to drift both upward and downward over the course of tens of milliseconds (Main et al. 2018).

4.4. Constraints on the Magneto-ionic Medium near FRB 121102

Plasma lensing, if relevant to the bursts' time–frequency structure, provides a constraint on the circum-source medium that adds to those previously derived from RM measurements (Michilli et al. 2018) and from the host galaxy's DM, DM$_{\rm host}$—as estimated from Hα measurements (Bassa et al. 2017; Kokubo et al. 2017; Tendulkar et al. 2017). We assume that all of the source-frame RM, RM$_{\rm src} = 1.46 \times 10^5 \, \mathrm{rad \, m^{-2}}$, is from a thin region near the source with thickness l but the associated DM$_{\rm RM}$ may be substantially less than DM$_{\rm host} \approx 100 \, \mathrm{pc \, cm^{-3}}$. These constrain the thickness and temperature of the Faraday region, as we now summarize briefly (see also Michilli et al. 2018).

We relate the parallel magnetic field estimated from RM$_{\rm src}$ to the magnetic pressure and obtain an electron density $n_e = 4.6 \times 10^4 \, \mathrm{cm^{-3}} \, \mathrm{DM}_{\rm RM,100}^{-2} F_g^{-1}$ in a region of thickness $l = 449 \, \mathrm{au} \times \mathrm{DM}_{\rm RM,100}^3 F_g$, where DM$_{\rm RM,100}$ is the DM associated with the Faraday medium in units of 100 pc cm^{-3}. The composite quantity $F_g \equiv \eta_B^2 T_4 / \beta$ is a "gas factor" comprising the temperature T_4 in units of $10^4 \, \mathrm{K}$, the plasma β (the ratio of thermal and magnetic energy densities with $\beta = 1$ in the case

---

[25] These variations are much larger and more rapid compared to the 10^{-2}–10^{-4} pc cm^{-3} variations seen over year-long timescales along normal pulsar lines of sight through the Galactic interstellar medium (Hobbs et al. 2004).

[26] Similar effects have also been seen in PSR B1744−24A (Bilous et al. 2011).

of equipartition), and a geometric factor $\eta_B \leqslant 1$ that accounts either for the misalignment of an ordered magnetic field from the line of sight or for a turbulent field with local values much larger than the net parallel component that determines RM. The corresponding free–free optical depth is $\tau_{\mathrm{ff}} \approx 1.5\, T_4^{-1.3}\, \nu^{-2.1}(F_{\mathrm{g}}\, \mathrm{DM}_{\mathrm{RM},100})^{-1}$. For a small DM in the Faraday region, e.g., $\mathrm{DM}_{\mathrm{RM}} = 1\,\mathrm{pc\,cm}^{-3}$, the optical depth is large even at 1 GHz unless the temperature or the composite gas factor F_{g} is also large.

If plasma lensing accounts for some of the time–frequency structure of the bursts, then the source's distance must exceed the focal distance given by Equation (7) of Cordes et al. (2017) for a Gaussian lens. Lensing occurring at a frequency ν_l in gigahertz requires $(a_{\mathrm{au}}\nu_l)^2/\mathrm{DM}_l d_{\mathrm{sl}} \leqslant 1.5\, d_{\mathrm{so}}$, where DM_l is the DM depth of the lens, a_{au} is the $1/e$ half width of the lens in astronomical units; d_{sl} and d_{so} are the source-lens and source-observer distances in parsecs and gigaparsecs, respectively. The path length through the lens is defined to be $l = Aa$, where A is a multiplier that allows nonspherical lenses to be considered. An upper bound on the depth is then

$$l \leqslant 24.5 \text{ au } (d_{\mathrm{sl}}d_{\mathrm{so}})^{1/2}\mathrm{DM}_{\mathrm{RM},100}^{1/2}\left(\frac{A}{\nu_l}\right). \qquad (1)$$

The combined constraints on l from DM, RM, and lensing give an upper bound on the gas factor

$$F_{\mathrm{g}} \leqslant 0.055\left(\frac{A}{\nu_l}\right)\frac{(d_{\mathrm{sl}}d_{\mathrm{so}})^{1/2}}{\mathrm{DM}_{\mathrm{RM},100}^{5/2}}, \qquad (2)$$

a lower bound on the electron density,

$$n_{\mathrm{e}} \geqslant 8.42 \times 10^5 \text{ cm}^{-3}\left(\frac{\mathrm{DM}_{\mathrm{RM},100}}{d_{\mathrm{so}}d_{\mathrm{sl}}}\right)^{1/2}\left(\frac{\nu_l}{A}\right), \qquad (3)$$

and a lower bound on the free–free optical depth,

$$\tau_{\mathrm{ff}} \geqslant 28.4\, T_4^{-1.3}\, \nu^{-2.1}\, \mathrm{DM}_{\mathrm{RM},100}^{3/2}(d_{\mathrm{so}}d_{\mathrm{sl}})^{-1/2}\left(\frac{\nu_l}{A}\right). \qquad (4)$$

Bursts at 8 GHz are qualitatively similar to those at lower frequencies, suggesting that lensing might be relevant at a wide range of frequencies. Using $\nu_l = 8$ GHz and requiring the region to be optically thin at $\nu = 1.5$ GHz, where most bursts have been detected, we require $\mathrm{DM}_{\mathrm{RM},100}^{3/2}/T_4^{1.3}A\sqrt{d_{\mathrm{sl}}} \lesssim 0.01$ (and possibly smaller given the inequality in Equation (4)). This can be satisfied by a small $\mathrm{DM}_{\mathrm{RM}}$, a large temperature or large A, or a source-lens distance larger than 1 pc. A reduced $\mathrm{DM}_{\mathrm{RM}}$ also makes the Faraday region thinner and less dense but more strongly magnetized. Furthermore, it substantially increases the upper bound on the gas factor.

Overall there appears to be sufficient latitude to account for the measured Faraday rotation as well as the requirements for plasma lensing. For a small $\mathrm{DM}_{\mathrm{RM}} = 1\,\mathrm{pc\,cm}^{-3}$, the Faraday region is very thin ($l \lesssim 1$–10 au), highly magnetized ($B \gtrsim 1$ G), and dense ($n_e \gtrsim 10^5\,\mathrm{cm}^{-3}$). Intriguingly, these values are comparable to those inferred for the Crab echo events, where Graham Smith et al. (2011) argued that these are created by plasma lensing from filaments with diameters of $\sim$2 au and electron density of the order of $10^4\,\mathrm{cm}^{-3}$.

The apparent increase of $\sim$1–3 $\mathrm{pc\,cm}^{-3}$ in FRB 121102's DM over 4 yr could indicate a genuine increase in electron column density along the line of sight, e.g., from an expanding supernova shock-wave sweeping up ambient material (Yang &

Zhang 2017; Piro & Gaensler 2018). However, we again caution that this is not necessarily a secular trend, and it could also reflect frequency-dependent arrival time delays due to variable plasma lensing like that seen in the Crab Nebula (Backer et al. 2000).

5. Conclusion and Future Work

We have shown that radio bursts detected from FRB 121102 often exhibit complex time–frequency structure that is unlike what is commonly seen in radio pulsars or radio-emitting magnetars. We apply a DM determination metric that maximizes structure in the frequency-averaged pulse profile, which reveals that the bursts are composed of temporally distinct subbursts with widths $\lesssim$1 ms and characteristic emission bandwidths of typically $\sim$250 MHz at $\sim$1.4 GHz. Furthermore, these subbursts drift to lower frequencies with time at a rate of $\sim$200 MHz ms^{-1} at 1.4 GHz, and the rate of drift is possibly larger at higher radio frequencies. We find that the bursts in this sample have a DM $= 560.57 \pm 0.07\,\mathrm{pc\,cm}^{-3}$ at MJD 57,644, and this suggests an increase of ΔDM $\sim$ 1–3 $\mathrm{pc\,cm}^{-3}$ in 4 yr. Whether this is a smooth, secular increase or whether there are stochastic variations at the $\sim$1 $\mathrm{pc\,cm}^{-3}$ level is, as yet, unclear.

We have discussed how the time–frequency structures in the bursts could be intrinsic to the emission mechanism, or due to local propagation effects. While the FRB 121102 bursts show many commonalities with the Crab pulsar high-frequency interpulses, the time–frequency structures are also consistent with plasma lensing, like that seen from the Crab Nebula and in the intrabinary material of PSR B1957+20. In either case, the time–frequency structure provides new information about the nature of the underlying bursting source and its environment. Overall, these new findings are consistent with previously proposed scenarios in which FRB 121102 is a particularly young neutron star in a dense nebula.

A larger, high-S/N, and broad frequency burst sample is needed to further address the nature of FRB 121102. In the absence of a prompt multiwavelength counterpart, the radio bursts themselves remain a key diagnostic. Future work can better quantify DM variations, whether the apparent drift rate of the subbursts changes with time, and whether there is a correlation between the variable RM and the time–frequency structure in the bursts. If the RM is dominated by a single plasma lens, correlated variations could be expected. Furthermore, a larger sample can address if subburst brightness is inversely proportional to its characteristic bandwidth and whether individual subbursts have demonstrably different DMs—both of which would be expected in a plasma lensing scenario. Continued monitoring, over the broadest possible range of radio frequencies, and preferentially with simultaneous ultrabroadband observations, is thus strongly motivated.

The low frequencies and huge fractional bandwidth (400–800 MHz) offered by CHIME (CHIME/FRB Collaboration et al. 2018) is well suited to exploring the role of local propagation effects like plasma lensing—especially if bursts can be studied in fine detail using coherent dedispersion on buffered voltage data. While FRB 121102 has yet to be detected below 1 GHz (Scholz et al. 2016), both UTMOST and CHIME have shown that FRBs are detectable at these frequencies (Boyle & CHIME/FRB Collaboration 2018; Farah et al. 2018). Finding commonalities or differences in the burst properties between repeating and apparently nonrepeating

FRBs may help establish whether they have a common physical origin or not. Indeed, during the refereeing stage of this Letter, the CHIME collaboration announced the discovery of a second source of repeating FRBs, whose burst properties look remarkably similar to those of FRB 121102 (CHIME/FRB Collaboration et al. 2019).

ORCID iDs

J. W. T. Hessels ⓘ https://orcid.org/0000-0003-2317-1446
L. G. Spitler ⓘ https://orcid.org/0000-0002-3775-8291
J. M. Cordes ⓘ https://orcid.org/0000-0002-4049-1882
R. S. Lynch ⓘ https://orcid.org/0000-0001-5229-7430
A. M. Archibald ⓘ https://orcid.org/0000-0003-0638-3340
G. C. Bower ⓘ https://orcid.org/0000-0003-4056-9982
F. Crawford ⓘ https://orcid.org/0000-0002-2578-0360
J. S. Deneva ⓘ https://orcid.org/0000-0003-1226-0793
V. Gajjar ⓘ https://orcid.org/0000-0002-8604-106X
V. M. Kaspi ⓘ https://orcid.org/0000-0001-9345-0307
B. Marcote ⓘ https://orcid.org/0000-0001-9814-2354
M. A. McLaughlin ⓘ https://orcid.org/0000-0001-7697-7422
Z. Paragi ⓘ https://orcid.org/0000-0002-5195-335X
E. Petroff ⓘ https://orcid.org/0000-0002-9822-8008
S. M. Ransom ⓘ https://orcid.org/0000-0001-5799-9714
S. P. Tendulkar ⓘ https://orcid.org/0000-0003-2548-2926

References

Backer, D. C., Wong, T., & Valanju, J. 2000, ApJ, 543, 740
Bannister, K. W., Stevens, J., Tuntsov, A. V., et al. 2016, Sci, 351, 354
Bassa, C. G., Beswick, R., Tingay, S. J., et al. 2016, MNRAS, 463, L36
Bassa, C. G., Tendulkar, S. P., Adams, E. A. K., et al. 2017, ApJL, 843, L8
Beloborodov, A. M. 2017, ApJL, 843, L26
Bilous, A. V., Ransom, S. M., & Nice, D. J. 2011, in AIP Conf. Ser. 1357, Radio Pulsars: An Astrophysical Key to Unlock the Secrets of the Universe, ed. M. Burgay (Melville, NY: AIP), 140
Boyle, P. C. & CHIME/FRB Collaboration 2018, ATel, 11901, 1
Caleb, M., Keane, E. F., van Straten, W., et al. 2018, MNRAS, 478, 2046
Champion, D. J., Petroff, E., Kramer, M., et al. 2016, MNRAS, 460, L30
Chatterjee, S., Law, C. J., Wharton, R. S., et al. 2017, Natur, 541, 58
CHIME/FRB Collaboration, Amiri, M., Bandura, K., et al. 2018, ApJ, 863, 48
CHIME/FRB Collaboration, Amiri, M., Bandura, K., et al. 2019, Natur, 566, 235
Clegg, A. W., Fey, A. L., & Lazio, T. J. W. 1998, ApJ, 496, 253
Connor, L., Sievers, J., & Pen, U.-L. 2016, MNRAS, 458, L19
Cordes, J. M., Bhat, N. D. R., Hankins, T. H., McLaughlin, M. A., & Kern, J. 2004, ApJ, 612, 375
Cordes, J. M., Freire, P. C. C., Lorimer, D. R., et al. 2006, ApJ, 637, 446
Cordes, J. M., & Lazio, T. J. W. 2002, arXiv:astro-ph/0207156
Cordes, J. M., & Wasserman, I. 2016, MNRAS, 457, 232
Cordes, J. M., Wasserman, I., Hessels, J. W. T., et al. 2017, ApJ, 842, 35
Cordes, J. M., Weisberg, J. M., & Boriakoff, V. 1985, ApJ, 288, 221
DeLaunay, J. J., Fox, D. B., Murase, K., et al. 2016, ApJL, 832, L1
DuPlain, R., Ransom, S., Demorest, P., et al. 2008, Proc. SPIE, 7019, 70191D
Eatough, R. P., Falcke, H., Karuppusamy, R., et al. 2013, Natur, 501, 391
Farah, W., Flynn, C., Bailes, M., et al. 2018, MNRAS, 478, 1209
Gajjar, V., Siemion, A. P. V., MacMahon, D. H. E., et al. 2017, ATel, 10675, 1
Gajjar, V., Siemion, A. P. V., Price, D. C., et al. 2018, ApJ, 863, 2
Gould, D. M., & Lyne, A. G. 1998, MNRAS, 301, 235
Graham Smith, F., Lyne, A. G., & Jordan, C. 2011, MNRAS, 410, 499
Hankins, T. H., & Eilek, J. A. 2007, ApJ, 670, 693
Hankins, T. H., Eilek, J. A., & Jones, G. 2016, ApJ, 833, 47
Hankins, T. H., & Rickett, B. J. 1975, MComP, 14, 55
Hardy, L. K., Dhillon, V. S., Spitler, L. G., et al. 2017, MNRAS, 472, 2800
Hobbs, G., Lyne, A. G., Kramer, M., Martin, C. E., & Jordan, C. 2004, MNRAS, 353, 1311
Jankowski, F., van Straten, W., Keane, E. F., et al. 2018, MNRAS, 473, 4436
Jessner, A., Popov, M. V., Kondratiev, V. I., et al. 2010, A&A, 524, A60
Johnston, S., Keane, E. F., Bhandari, S., et al. 2017, MNRAS, 465, 2143
Kaneda, K., Misawa, H., Iwai, K., Tsuchiya, F., & Obara, T. 2015, ApJL, 808, L45
Kashiyama, K., & Murase, K. 2017, ApJL, 839, L3
Keane, E. F., Johnston, S., Bhandari, S., et al. 2016, Natur, 530, 453
Kokubo, M., Mitsuda, K., Sugai, H., et al. 2017, ApJ, 844, 95
Kramer, M., Karastergiou, A., Gupta, Y., et al. 2003, A&A, 407, 655
Law, C. J., Abruzzo, M. W., Bassa, C. G., et al. 2017, ApJ, 850, 76
Lazaridis, K., Jessner, A., Kramer, M., et al. 2008, MNRAS, 390, 839
Lazarus, P., Brazier, A., Hessels, J. W. T., et al. 2015, ApJ, 812, 81
Lorimer, D. R., Bailes, M., McLaughlin, M. A., Narkevic, D. J., & Crawford, F. 2007, Sci, 318, 777
Lorimer, D. R., & Kramer, M. 2004, Handbook of Pulsar Astronomy (Cambridge: Cambridge Univ. Press)
Lu, W., & Kumar, P. 2018, MNRAS, 477, 2470
Lyubarsky, Y. 2014, MNRAS, 442, L9
Lyutikov, M. 2017, ApJL, 838, L13
Lyutikov, M., Burzawa, L., & Popov, S. B. 2016, MNRAS, 462, 941
Main, R., Yang, I.-S., Chan, V., et al. 2018, Natur, 557, 522
Marcote, B., Paragi, Z., Hessels, J. W. T., et al. 2017, ApJL, 834, L8

Margalit, B., Metzger, B. D., Berger, E., et al. 2018, MNRAS, 481, 2407
Masui, K., Lin, H., Sievers, J., et al. 2015, Natur, 528, 523
Metzger, B. D., Berger, E., & Margalit, B. 2017, ApJ, 841, 14
Michilli, D., Seymour, A., Hessels, J. W. T., et al. 2018, Natur, 553, 182
Murase, K., Kashiyama, K., & Mészáros, P. 2016, MNRAS, 461, 1498
Osten, R. A., & Bastian, T. S. 2006, ApJ, 637, 1016
Osten, R. A., & Bastian, T. S. 2008, ApJ, 674, 1078
Petroff, E., Bailes, M., Barr, E. D., et al. 2015a, MNRAS, 447, 246
Petroff, E., Barr, E. D., Jameson, A., et al. 2016, PASA, 33, e045
Petroff, E., Johnston, S., Keane, E. F., et al. 2015b, MNRAS, 454, 457
Piro, A. L. 2016, ApJL, 824, L32
Piro, A. L., & Gaensler, B. M. 2018, ApJ, 861, 150
Popov, S. B., & Postnov, K. A. 2013, arXiv:1307.4924
Ransom, S. M. 2001, PhD thesis, Harvard Univ.
Ravi, V. 2019, MNRAS, 482, 1966
Ravi, V., Shannon, R. M., Bailes, M., et al. 2016, Sci, 354, 1249
Ravi, V., Shannon, R. M., & Jameson, A. 2015, ApJL, 799, L5
Ryabov, V. B., Zarka, P., Hess, S., et al. 2014, A&A, 568, A53
Savitzky, A., & Golay, M. J. E. 1964, AnaCh, 36, 1627

Scholz, P., Bogdanov, S., Hessels, J. W. T., et al. 2017, ApJ, 846, 80
Scholz, P., Spitler, L. G., Hessels, J. W. T., et al. 2016, ApJ, 833, 177
Shannon, R. M., Macquart, J.-P., Bannister, K. W., et al. 2018, Natur, 562, 386
Spitler, L. G., Cordes, J. M., Hessels, J. W. T., et al. 2014, ApJ, 790, 101
Spitler, L. G., Herrmann, W., Bower, G. C., et al. 2018, ApJ, 863, 150
Spitler, L. G., Scholz, P., Hessels, J. W. T., et al. 2016, Natur, 531, 202
Tendulkar, S. P., Bassa, C. G., Cordes, J. M., et al. 2017, ApJL, 834, L7
Thornton, D., Stappers, B., Bailes, M., et al. 2013, Sci, 341, 53
Treumann, R. A. 2006, A&ARv, 13, 229
van Straten, W., & Bailes, M. 2011, PASA, 28, 1
van Straten, W., Demorest, P., & Oslowski, S. 2012, AR&T, 9, 237
Watson, P. G., & Melrose, D. B. 2006, ApJ, 647, 1142
Waxman, E. 2017, ApJ, 842, 34
Williams, P. K. G., & Berger, E. 2016, ApJL, 821, L22
Yang, Y.-P., & Zhang, B. 2017, ApJ, 847, 22
Yao, J. M., Manchester, R. N., & Wang, N. 2017, ApJ, 835, 29
Zarka, P. 1992, AdSpR, 12, 99
Zhang, Y. G., Gajjar, V., Foster, G., et al. 2018, ApJ, 866, 149